*photonics*

MDPI

*Article*

# Research on Polarization Defogging Imaging Algorithm for Long-Distance Targets Based on Improved Semi-Inverse Principle

**Qiang Song [1], Ming Zhao [1,*], Deshuo Meng [1], Taiping Yang [1] and Youwen Sun [2]**

[1] School of Electronic Engineering, Huainan Normal University, Huainan 232038, China; song2023@hnnu.edu.cn (Q.S.); mengdeshuo@126.com (D.M.); tpyang@hnnu.edu.cn (T.Y.)
[2] State Key Laboratory of Opto-Electronic Information Acquisition and Protection Technology, Anhui University, Hefei 230601, China; ywsun@ahu.edu.cn
* Correspondence: zhaom@hnnu.edu.cn

**Abstract**

To address problems such as inaccurate atmospheric light estimation, color distortion, and insufficient preservation of edge details in traditional dehazing algorithms under haze conditions, this paper proposes a color polarization dehazing algorithm based on an improved semi-inverse principle. First, the semi-inverse principle is deeply integrated with the physical model of polarization imaging. By constructing a semi-inverse transformation model in the polarization space, pixel-level adaptive estimation of atmospheric light parameters is achieved. Second, median filtering is used to estimate the atmospheric light intensity to suppress abnormal highlight noise, and the lower bound of transmittance is appropriately raised to preserve weak signals from distant objects. Then, the transmittance is estimated based on the relationship between the polarization difference within a sky mask and the degree of polarization of atmospheric light. Guided filtering is further employed to refine the transmittance map, and an enhancement factor and gamma correction are introduced to compensate for brightness loss and improve visibility in dark areas. Finally, a local detail enhancement module is used to restore details in hazy regions, thereby improving the overall contrast of the image. Experimental results on real hazy images demonstrate that the proposed algorithm outperforms classical polarization-based dehazing methods and mainstream single-image dehazing algorithms in both subjective visual quality and objective metrics. In particular, the restoration capability for distant targets is significantly enhanced, effectively solving the problem of distant target disappearance.

**Keywords:** semi-inverse principle; polarization imaging; image dehazing; atmospheric light estimation; transmittance optimization

Check for updates

Received: 2 September 2026
Revised: 6 October 2026
Accepted: 20 October 2026
Published: 26 October 2026

**Copyright:** © 2026 by the authors. Licensee MDPI, Basel, Switzerland. This article is an open access article distributed under the terms and conditions of the Creative Commons Attribution (CC BY) license.

## 1. Introduction

The atmospheric scattering effect caused by hazy weather is a key factor that restricts the imaging quality of outdoor optical imaging systems [1]. Affected by multiple scattering from suspended particles in the atmosphere, captured images commonly suffer from degradation problems such as contrast reduction, color distortion, and detail blurring, which significantly impair the performance of subsequent high-level vision tasks including target recognition and scene understanding [2]. Therefore, developing efficient and robust image dehazing methods holds significant theoretical research value and practical engineering application significance [3].

Underground imaging suffers from severe haze, color distortion and uneven illumination induced by coal dust and water mist. Existing underground dehazing approaches adopt domain-specific designs but mostly rely on intensity priors without exploiting polarization information. Traditional single-image dehazing methods such as the linear-transformation-based algorithm [4] only restore 2D visual quality and fail to reconstruct 3D geometry under scattering. Deep learning advances include exposure difference networks for low-light enhancement [5] and depth-completion frameworks, as well as joint dehazing-depth networks. However, these methods are mainly developed for automotive or indoor scenes and seldom adapted to underground turbid media. Polarization provides an extra physical dimension to decode scene structure from scattered light [6]. Recent studies have validated passive polarization stereo [7], polarimetric binocular imaging in turbid water [8], and polarization-guided networks embedding differentiable physical constraints for joint descattering and 3D recovery [9]. These works represent the trend of data-driven polarimetric imaging combining physical priors and deep learning [10,11], inspiring our polarization dehazing framework for underground scattering scenes.

Among traditional dehazing algorithms, the dark channel prior proposed by He et al. [12] achieved a breakthrough by estimating atmospheric light and transmission effectively based on the statistical property that, within a local patch of a haze-free image, at least one color channel exhibits very low intensity. However, the dark channel prior may fail in sky regions or areas containing white objects. Schechner et al. [13] combined polarization imaging with the atmospheric scattering model and proposed the classic polarization-based dehazing method. Nevertheless, traditional polarization dehazing methods typically require manual selection of sky regions to estimate the polarimetric parameters of atmospheric light, are sensitive to the polarization characteristics of target objects, and tend to suffer from noise amplification in scenes with a low degree of polarization. Liang et al. [14] integrated polarization information with the dark channel prior to improve the robustness of atmospheric light estimation. Feng et al. [15] proposed a transmission optimization method guided by the degree of polarization, suppressing noise through guided filtering. However, existing methods still have room for improvement in terms of color fidelity and edge detail preservation. Zhao et al. [16] proposed a novel atmospheric light estimation method based on polarization degree gradient, which accurately locates valid sky regions and effectively avoids the inaccurate atmospheric light calculation caused by complex foreground interference. Li et al. [17] proposed a polarization dehazing method for sea fog images based on pixel-level skylight polarization degree estimation, which addresses the spatial variation in skylight polarization degree in sea fog scenes and achieves reliable haze removal for sea fog images.

In recent years, dehazing methods that fuse multiple priors have become a research focus. Combining physical models with statistical priors can overcome the limitations of a single prior. For example, fusing the dark channel prior with the color attenuation prior can improve the processing of sky regions, while combining polarization information with depth information can enhance dehazing quality in areas with abrupt depth variations. The semi-inverse dehazing algorithm proposed by Ancuti et al. [18] originates from the algebraic inversion of the atmospheric scattering model and is a physically driven method that does not rely on statistical priors such as the dark channel prior. Traditional dehazing algorithms mostly estimate transmission based on empirical assumptions, whereas the semi-inverse method directly performs mathematical inversion on the imaging model, hence the term "semi-inverse". Its core idea is, given the atmospheric light, to apply a semi-inverse transformation to the imaging equation to obtain initial estimates of the transmission and the haze-free image; the results are then refined through smoothness constraints, edge preservation, and other regularizations to avoid noise amplification and distortion

caused by direct inversion. This method is simple in principle and computationally efficient, enabling stable dehazing without dependence on complex priors, and thus provides a foundational solution framework for subsequent improved algorithms that integrate polarization, guided filtering, and the like. The constraints imposed by the semi-inverse principle in color space can compensate for the deficiencies of polarization methods in low-polarization regions, while polarization information can supply semi-inverse-based methods with more accurate atmospheric light estimation. It is precisely based on this idea that this paper deeply integrates an improved semi-inverse principle with color polarimetric imaging to achieve superior long-range imaging performance.

To address the above issues, this paper combines the semi-inverse principle with polarization imaging techniques and proposes a color polarimetric dehazing algorithm based on an improved semi-inverse principle. The main contributions are as follows: a semi-inverse transformation model in polarization space is constructed, and the Stokes parameters are utilized to achieve adaptive estimation of the polarization characteristics of atmospheric light, thereby avoiding the dependence on manual region selection in traditional methods; a refined transmission estimation method based on guided filtering is designed, which integrates the advantages of polarization difference and the semi-inverse prior to effectively suppress noise amplification in low-polarization regions; and a color fidelity constraint is introduced to significantly improve the color restoration quality of dehazed images.

## 2. Theoretical Basis of Polarization Imaging and Atmospheric Scattering

Under haze conditions, the light intensity received by a camera consists of two components: the direct component of the target-reflected light that has been attenuated by the atmosphere, and the component of sunlight scattered by atmospheric aerosols [19,20]. The atmospheric scattering model can be expressed as:

$$I(x) = L_{direct}(x) + L_{scatter}(x) = J(x) * t(x) + A_{\infty}(1 - t(x)) \tag{1}$$

where $I(x)$ is the total light intensity received by the camera, $J(x)$ is the target radiance in haze-free conditions, $t(x) = e^{-\beta d(x)}$ is the transmission, and $A_{\infty}$ is the atmospheric light intensity at infinity. This model assumes that atmospheric scattering is homogeneous, and that the scattering coefficient is wavelength-dependent but does not vary with spatial position. It can be seen from the model that the core of dehazing lies in estimating the transmission $t(x)$ and the atmospheric light $A_{\infty}$. Once these two parameters are accurately estimated, the target radiance can be recovered as [21]:

$$J(x) = (I(x) - A_{\infty}(1 - t(x)))/t(x) \tag{2}$$

The polarization state of light can be described by the Stokes vector $S = [S_0\ S_1\ S_2\ S_3]^T$, where $S_0$ denotes the total light intensity, $S_1$ represents the difference between the horizontally and vertically polarized components, $S_2$ is the difference between the 45° and 135° polarized components, and $S_3$ corresponds to the difference between the left- and right-handed circularly polarized components. In practical applications, atmospheric scattering is mainly concerned with the linear polarization component, while the circular polarization component is usually neglected. By acquiring polarization images at four orientations of 0°, 45°, 90°, and 135°, the Stokes parameters can be calculated. The degree of linear polarization (DoLP) and the angle of polarization (AoP) can be expressed as [22]:

$$\begin{cases} DoLP = (\sqrt{S_1^2 + S_2^2})/S_0 \\ AoP = \frac{1}{2} * \arctan(S_2/S_1) \end{cases} \tag{3}$$

In the polarization-based dehazing model, it is assumed that the atmospherically scattered light exhibits a high degree of polarization, while the target-reflected light is approximately unpolarized. Based on this assumption, images acquired at different polarization orientations can be expressed as [23]:

$$\begin{cases} I_{//}(x) = \frac{J(x)t(x)}{2} + \frac{A_\infty(1-t(x))}{2} + \frac{A_\infty(1-t(x))P_A}{2} \\ I_\perp(x) = \frac{J(x)t(x)}{2} + \frac{A_\infty(1-t(x))}{2} - \frac{A_\infty(1-t(x))P_A}{2} \end{cases} \tag{4}$$

where $P_A$ denotes the degree of polarization of the atmospheric light, $I_{//}$ and $I_\perp$ represent the polarization images whose polarization directions are parallel and perpendicular to the polarization direction of the atmospheric light, respectively, which also correspond to the maximum and minimum intensity components. The scattered light component obtained by subtracting orthogonal images can be expressed as:

$$I_{//}(x) - I_\perp(x) = A_\infty(1 - t(x))P_A \tag{5}$$

The transmission can then be derived as:

$$t(x) = 1 - \frac{I_{//}(x) - I_\perp(x)}{A_\infty P_A} \tag{6}$$

Conventional methods typically require manual selection of the sky region to estimate $A_\infty$ and $P_A$, which limits the automation and robustness of the algorithm.

## 3. Improved Semi-Inverse Principle and Color Polarization Dehazing Algorithm

### *3.1. Luminance Map and Semi-Inverse Mask Extraction*

In a local patch $\Omega$ of a haze-free image, the surface reflectance color vector $J_c(x)$ and the atmospheric light vector **A** lie on a plane in the RGB space. In a hazy image, the observed vector $I_c(x)$ can be expressed as [24]:

$$I_c(x) = t(x)J_c(x) + (1 - t(x))A \tag{7}$$

According to Equation (7), the observed color $I_c(x)$ is a linear interpolation between the scene radiance $J_c(x)$ and the atmospheric light $A$. As the transmission $t(x)$ decreases from 1 to 0, $I_c(x)$ moves from $J_c(x)$ toward $A$. Hence, $I_c(x)$ lies on the segment between $J_c(x)$ and $A$, rather than between the origin and $A$. The semi-inverse transform is defined as:

$$I_{inv}(x) = A - I(x) \tag{8}$$

where $A$ is the Stokes vector of atmospheric light, and $I(x)$ denotes the observed Stokes vector of the hazy pixel at spatial position $x$. This transformation builds a feature space that highlights sky-region polarization characteristics. Combined with morphological operations, we generate the sky mask $M_{sky}$, which is then used to estimate atmospheric light intensity $A_\infty$ and atmospheric polarization degree $p_A$.

In the semi-inverse space, the distribution of hazy pixels exhibits a specific geometric structure. By analyzing the degree of aggregation of pixels in the semi-inverse image, the atmospheric light vector **A** can be estimated. The conventional semi-inverse principle has the following problems in its implementation: first, the estimation of the atmospheric light vector relies on the statistical properties of pixels within local patches, which tends to produce deviations in regions with complex textures; second, it fails to consider the polar-

ization characteristics of atmospheric scattering, resulting in imprecise estimation of the haze density; and finally, it lacks an effective constraint mechanism for color restoration.

To obtain a reliable region for estimating the atmospheric light, for each color channel c ∈ {R, G, B}, the corresponding channel is extracted from the four polarization images. First, a composite luminance map $I_{gray}$ is computed as:

$$I_{\text{gray}} = \frac{1}{12}\sum_{c=1}^{3}\left(I_0^{(c)} + I_{45}^{(c)} + I_{90}^{(c)} + I_{135}^{(c)}\right) \tag{9}$$

This equation averages over all color channels and the four polarization angles, representing the overall luminance distribution of the scene. Let $L = I_{\text{gray}}$; the semi-inverse image is defined as:

$$H(x) = \min(L(x), 1 - L(x)) \tag{10}$$

Because hazy regions typically have luminance values tending toward a middle value (around 0.5), the value of H is usually large, whereas in bright sky areas or on dark objects, H is small. Here, an adaptive threshold T = 0.8 × max(H) is selected to obtain an initial sky/haze mask, as expressed in the following equation:

$$M_{\text{init}}(x) = (H(x) > T) \wedge (L(x) > 0.45) \tag{11}$$

where $L(x) > 0.45$ further excludes falsely detected overly dark regions. If the area of the mask $M_{\text{init}}$ is less than 1% of the total number of pixels, the threshold is lowered to $T = 0.6 \times \max(H)$, the luminance threshold is adjusted to 0.4, and the mask is recomputed. A morphological closing operation is then applied to $M_{\text{init}}$ by using a circular structuring element with a radius of 5 (dilation followed by erosion) to fill holes and connect adjacent regions, yielding the sky mask $M_{\text{sky}}$ used for the subsequent estimation of the atmospheric light parameters.

$$M_{\text{sky}} = \text{imclose}(M_{init}, \text{disk}(5)) \tag{12}$$

### *3.2. Spatial Variation in the Degree of Polarization of Atmospheric Backscattered Light*

Within the sky mask $M_{\text{sky}}$, the set of total intensity pixels $\{I_{\text{total}}(x) \mid M_{\text{sky}}(x) = 1\}$ is extracted. Conventional methods use the mean, which is susceptible to interference from abnormally bright pixels [25]. This paper adopts the median to estimate the atmospheric light intensity, so as to suppress the influence of abnormally bright noise within the sky region, as expressed in Equation (13):

$$A_\infty = \begin{cases} \text{median}(I_{\text{sky}}), & if \quad N_{sky} \geq 100 \\ \text{median}(Top_{0.5\%}(I)), & otherwise \end{cases} \tag{13}$$

If the number of pixels inside the mask is less than 100 (an extreme case), the estimate falls back to the median of the brightest 0.5% pixels in the entire image. Finally, a lower bound constraint is imposed, as shown in Equation (14):

$$A_\infty = \max(A_\infty, 0.3) \tag{14}$$

This lower bound constraint ensures that even if the overall scene is dark, the atmospheric light will not be too low, thereby avoiding negative values in the transmission calculation.

In hazy imaging, atmospheric scattering is dominated by aerosol backscattering. The polarization state of the scattered light is jointly determined by the number of scattering events, aerosol particle size, and scattering angle: for close-range scenes, atmospheric scattering is primarily single scattering, where photons follow a single scattering path, result-

ing in a regular polarization state and a high degree of polarization; as the target distance increases, multiple scattering becomes dominant in the atmosphere, and after undergoing multiple random scattering events, the original polarization state of photons is completely scrambled, leading to a pronounced depolarization effect and a substantial decrease in the degree of polarization of the scattered light.

To address the deficiencies of the conventional constant-polarization-degree assumption, and by incorporating the mechanism of aerosol multiple-scattering depolarization, a spatial evolution model of the degree of polarization of backscattered light $p_A(x)$ is established. According to the Beer–Lambert Law, when light propagates through scattering media such as fog and water, the light intensity decays exponentially with distance $d(x)$:

$$I(x) = I_0 \cdot e^{-\beta d(x)} \tag{15}$$

where $\beta$ denotes the extinction coefficient.

The definition of the degree of polarization (DoP) relies on the ratio of the polarized component to the total intensity within Stokes parameters:

$$p = \frac{\sqrt{Q^2 + U^2 + V^2}}{I} \tag{16}$$

As light propagates through the medium, multiple scattering continuously generates unpolarized light, which causes the polarized component $I_p = \sqrt{Q^2 + U^2 + V^2}$ to decay faster than the total intensity $I$. Let $p(d)$ be the degree of polarization at distance $d$. Owing to the depolarization effect, the decay rate of the degree of polarization along the propagation path is proportional to the current polarization state:

$$\frac{dp(d)}{dd} = -\alpha \cdot p(d) \tag{17}$$

where $\alpha > 0$ is the depolarization coefficient, representing the rate of depolarization induced by multiple scattering within the medium.

Solving the above differential equation yields the exponential relationship between depolarization and propagation distance:

$$p_A(x) = p_0 \cdot e^{-\alpha \cdot d(x)} \tag{18}$$

where $p_0$ is the initial degree of polarization of near-ground atmospheric scattered light, determined by the physical properties of the aerosol; $\alpha$ is the polarization depolarization coefficient, which is positively correlated with fog concentration and aerosol particle size distribution; and $d(x)$ is the target imaging distance. Equation (18) indicates that the degree of polarization decays exponentially with propagation distance due to multiple scattering. The physical characteristics of Equation (18) are analyzed as follows:

In the close-range region ($d(x) \to 0$): $e^{-\alpha d(x)} \approx 1$, $p_A(x) \approx p_0$; the degree of polarization approaches its initial value, the polarization information is intact and reliable, and the transmission estimation achieves high accuracy. In the distant region ($d(x) \to \infty$): multiple scattering effects become significant, $e^{-\alpha d(x)} \to 0$, $p_A(x) \to 0$; the scattered light is completely depolarized, the polarization information fails, and the transmission estimation based on polarization differences suffers from severe errors. The higher the fog concentration, the larger the depolarization coefficient $\alpha$; consequently, at the same distance, the decay of $p_A(x)$ is faster, and the distance at which polarization information becomes invalid is shorter.

The depolarization model in Equation (18) is physically motivated by the multiple-scattering effect in fog. As light propagates through fog, cumulative scattering events depo-

larize the atmospheric light, and the atmospheric polarization degree decays exponentially with distance. This model is only valid within the effective polarization detection distance.

In implementation, we introduce a minimum threshold $P_{A,\min}$ for $P_A(x)$. When $P_A(x) > P_{A,\min}$, the estimated atmospheric polarization is reliable and adopted for transmission estimation in Equation (6). When $P_A(x) \leq P_{A,\min}$, $P_A(x)$ is clamped to $P_{A,\min}$. In this far-range regime, polarization information is no longer trusted, and the physically derived transmission lower bound $t_{\min}$ dominates to constrain transmission and avoid excessive attenuation of target signals.

The DoP of the atmospheric light is defined as the average ratio of the polarization difference intensity to the total intensity within the sky region, and can be expressed as:

$$p_A = \frac{\text{mean}\left\{ I_{diff}(x) \middle| M_{sky}(x) = 1 \right\}}{A_\infty + \varepsilon} \tag{19}$$

where $\varepsilon = 10^{-6}$ prevents division by zero. In implementation, the image is divided into overlapping local patches. For each patch, $p_A$ is calculated individually using the sky mask $M_{sky} = 1$ within this patch. Different patches yield different $p_A$ values, which realizes the spatially varying atmospheric polarization described in Equation (15). The fixed transmission floor $t_{\min} = 0.35$ is applied to all pixels as an independent safety constraint and does not remove the spatial variation in the solved transmission map. To avoid outliers, $p_A(x)$ is clipped to a reasonable range:

$$p_A = \max(0.2, \min(0.95, p_A)) \tag{20}$$

In actual scenes, the DoP of atmospheric light typically lies between 0.2 and 0.9, a range that covers the majority of cases.

### *3.3. Transmission Estimation and Physical Quantitative Modeling of the Transmission Lower Bound*

Based on the atmospheric scattering model and the polarization separation principle [26], the transmission expression in Equation (6) can be rewritten as:

$$t(x) = 1 - \frac{I_{diff}(x)}{p_A \cdot A_\infty + \varepsilon} \tag{21}$$

The physical meaning of this expression is that the polarization difference intensity primarily originates from atmospheric light scattering. In the ideal physical case without the $p_A$ clipping in Equation (20), atmospheric polarization degree $p_A$ tends to zero for targets far beyond the effective polarization detection distance. Even tiny noise in the measured polarization difference $I_{diff}$ will make the term $I_{diff}/(p_A A_\infty)$ diverge, yielding non-physical negative transmission values, which is the core failure of polarization-based transmission estimation. After applying the $p_A$ lower bound in Equation (20), $p_A$ is clamped to 0.2. When $I_{diff} \to 0$, the numerical calculation gives $t(x) \to 1$, which is merely a bounded numerical behavior rather than the true physical limit. To handle this physical failure, we introduce the transmission lower bound to constrain transmission within a physically reasonable range when polarization information loses reliability.

To prevent the transmission from becoming too small and causing complete attenuation of distant targets, it is set as follows:

$$t(x) = \max(t_{\min}, \min(t_{\max}, t(x))) \tag{22}$$

Traditional methods often set a fixed lower bound $t_{\min}$ = 0.1, which results in extremely low brightness and loss of detail in restored regions with large depth of field. Experiments show that raising the lower bound to 0.35 can achieve a good balance between preserving weak signals and avoiding excessive haze. To prevent division-by-zero overflow caused by the transmission approaching zero, traditional algorithms usually adopt a fixed empirical value $t_{\min}$ (e.g., 0.3 or 0.35). Such values lack physical justification and cannot adapt to scenes with different fog concentrations and imaging distances: when the fog concentration is high, the fixed value of $t_{\min}$ is too small and cannot prevent distant targets from disappearing; when the fog concentration is low, the fixed value $t_{\min}$ is too large, leading to over-bright images and distorted details. Therefore, it is necessary to establish a quantitative relationship between the transmission lower bound and atmospheric physical parameters to realize an adaptive physical constraint. Based on the spatial evolution law of the degree of polarization of backscattered light, the effective polarization detection distance $d_p$ is defined as follows: when the degree of polarization of backscattered light $p_A(x)$ attenuates to the minimum detectable degree of polarization $p_{\min}$ of the imaging system, the corresponding target distance is the effective polarization detection distance. At this point, the polarization information drops to the system detection threshold; in regions beyond this distance, the polarization information becomes completely invalid and cannot be used for accurate transmission estimation. Substituting the minimum detectable degree of polarization $p_A(x) = p_{\min}$ into Equation (18), the effective polarization detection distance can be derived as [27]:

$$d_p = \frac{1}{\alpha} \ln\left(\frac{p_0}{p_{\min}}\right) \tag{23}$$

where $p_{\min}$ is an intrinsic parameter of the imaging system, determined by the detection sensitivity and noise level of the polarization camera. From Equation (23), it can be seen that as fog concentration of $\alpha$ increases, the effective polarization detection distance of $d_p$ decreases, and the region of polarization failure expands at longer ranges.

Substituting the effective polarization detection distance $d_p$ into the Beer–Lambert transmission formula yields the transmission lower bound $t_{\min}$ with rigorous physical meaning, which is the minimum transmission constraint value for the region where polarization fails:

$$t_{\min} = e^{-\beta d_p} \tag{24}$$

By combining Equation (23) and Equation (24), the quantitative physical model relating the transmission lower bound to fog concentration, depolarization coefficient, and system detection performance is finally established, as shown in Equation (25):

$$t_{\min} = \exp\left(-\frac{\beta}{\alpha} \ln \frac{p_0}{p_{\min}}\right) \tag{25}$$

The characteristics of this physical model are analyzed as follows: $t_{\min}$ is not an empirical constant, but a physical quantity determined jointly by the fog concentration $\beta$, the polarization depolarization coefficient $\alpha$, the minimum detectable degree of polarization of the system $p_{\min}$, and the initial degree of polarization $p_0$, and it can be adaptively calculated based on the atmospheric parameters of the scene. The higher the fog concentration (the larger $\beta$), the stronger the depolarization effect (the larger $\alpha$), and the larger the required value of $t_{\min}$. When the target distance exceeds the effective polarization detection distance $d_p$, the lower bound $t_{\min}$can effectively constrain the transmission, preventing excessive attenuation and ensuring that the target signal is not annihilated. By integrating the atmospheric scattering model and the polarization depolarization effect, the physical essence of raising the transmission lower bound to restore distant targets is revealed from two dimensions: signal fidelity and model deviation compensation. In distant scenes, the

backscattered light is completely depolarized $p_A(x) \to 0$. From Equation (23), the polarization difference intensity $D(x)$ approaches 0, and the estimated transmission $t(x) \to 0$. At this point, the denominator in Equation (24) approaches 0. Even if a weak valid signal exists from the target, it will be excessively amplified due to the excessively small denominator, and ultimately truncated to zero due to numerical overflow, manifesting as distant targets turning completely black with loss of details.

In this paper, a lower bound constraint is imposed on the transmission for distant regions through the physical quantitative model, and its physical essence of $t_{\min}$ is manifested in three aspects. First, it compensates for the model deviation caused by the failure of polarization information. In distant regions, multiple scattering renders the polarization information completely invalid, and the transmission estimated based on polarization has no physical reference significance. Serving as a physical constraint, $t_{\min}$ replaces the biased transmission estimate, thereby ensuring the numerical stability of the image restoration formula. Second, it protects the weak signal of distant targets. By constraining the minimum value of the transmission, the denominator in the restoration formula is prevented from approaching zero, preserving the weak but valid signal reflected from the target and avoiding over-amplification or truncation of the signal, thus recovering the contours and texture details of distant targets. Third, it adapts to the physical laws of atmospheric scattering. $t_{\min}$ adjusts adaptively with the fog concentration and imaging distance, which not only guarantees the restoration quality of distant targets but also avoids image distortion in the near-field region caused by an overly strong transmission constraint, achieving physical consistency in full-scene imaging.

The initial transmission map $t(x)$ may suffer from block artifacts, and its texture edges are not sufficiently sharp. Guided filtering is adopted to refine $t(x)$. The guided filter assumes that, within a local window of $\omega_k$, the output of $q$ is a linear transformation of the guidance image, and is expressed as [12]:

$$q_i = a_k I_i + b_k, \forall i \in \omega_k \tag{26}$$

By minimizing the reconstruction error with a regularization term, the coefficients are obtained as:

$$E(a_k, b_k) = \sum_{i \in \omega_k} \left( (a_k I_i + b_k - t_i)^2 + \varepsilon a_k^2 \right) \tag{27}$$

where $\varepsilon$ is a smoothing parameter. Solving the equation gives:

$$a_k = \frac{\frac{1}{|\omega|}\sum_{i \in \omega_k} I_i t_i - \mu_k \overline{t_k}}{\sigma_k^2 + \varepsilon}, \; b_k = \overline{t_k} - a_k \mu_k \tag{28}$$

The final output is given by $q_i = \overline{a_i} I_i + \overline{b_i}$, where $\overline{a_i}$ and $\overline{b_i}$ denote the mean values of the coefficients $a_k$ and $b_k$ over all windows that contain pixel $i$. In this paper, the filter radius is set to $r = 50$, and the regularization parameter is set to $\varepsilon = 10^{-3}$.

In summary, the transmission lower bound is no longer merely a numerical constraint; rather, it serves as a physical compensation mechanism for the depolarization effect caused by scattering in foggy conditions. This fundamentally resolves, from the perspective of atmospheric scattering, the core issue of distant targets vanishing in conventional algorithms, and lays a theoretical foundation for the subsequent rapid enhancement algorithm based on median filtering and polarization modulation. Its corresponding physical implication is that for the scenes in our experiments, when the attenuation coefficient does not exceed 0.034 and the target distance does not exceed 30 m, the physical transmission is guaranteed to remain above 0.35. For scenes outside this range, users may adjust the bound according to the above formula based on the actual fog density and distance. By anchoring the

fixed empirical parameter to the physical model, the proposed method strikes a balance between practicality and physical rigor.

### *3.4. Image Restoration and Enhancement*

Substituting the estimated atmospheric light of $A_\infty$ and the refined transmission map of $t_{\text{guided}}(x)$ into the atmospheric scattering model and yields:

$$J(x) = \frac{I_{\text{total}}(x) - A_\infty(1 - t_{\text{guided}}(x))}{\mu \cdot t_{\text{guided}}(x) + \varepsilon} \tag{29}$$

where a small constant of $\delta$ is used to prevent division by zero. The coefficient $\mu$ is defined as an adjustment factor, which can be greater or less than 1 according to the scene. The guided transmission $t_{\text{guided}}(x)$ is constrained by a physical lower bound and becomes overestimated for distant foggy regions. The adjustment factor $\mu$ is introduced to calibrate this systematic bias of transmission. For the foggy scenes in this work, $\mu = 2.3$. The joint effect of $\mu$ and the biased $t_{\text{guided}}(x)$ compensates the brightness attenuation of distant targets.

To further enhance shadow details, gamma correction is applied to the restored image, as given by:

$$J_{\text{gamma}}(x) = (\max(0,\min(1,J(x))))^{\gamma} \tag{30}$$

In this paper, $\gamma = 0.7$ is adopted. Since this value is less than 1, it stretches the dynamic range of dark regions, thereby enhancing the contrast of distant objects. After correction, the overall brightness distribution of the image becomes more uniform.

Although the above dehazing processing recovers most of the image textures, fine details in dense haze regions may still remain blurred. To tackle this issue, CLAHE with a low clip-limit constraint is adopted for post-enhancement. Unlike conventional CLAHE, a relatively low clip limit of 0.015 (normalized within [0, 1]) is set in our work to suppress noise amplification. The image is transformed into the LAB color space, and the CLAHE operation is only applied on the L (lightness) channel. For each $8 \times 8$ tile, the local histogram is calculated; pixels exceeding the clip limit are clipped, and the excess pixel counts are uniformly redistributed across the histogram. Bilinear interpolation is utilized to eliminate block artifacts between adjacent tiles. Finally, the enhanced L channel is combined with the original A and B channels. This strategy effectively recovers subtle textures in distant hazy regions while avoiding excessive noise amplification, and outputs the final clear haze-free image. The overall workflow of the proposed color polarization dehazing algorithm based on the improved semi-inverse principle is illustrated in Figure 1.

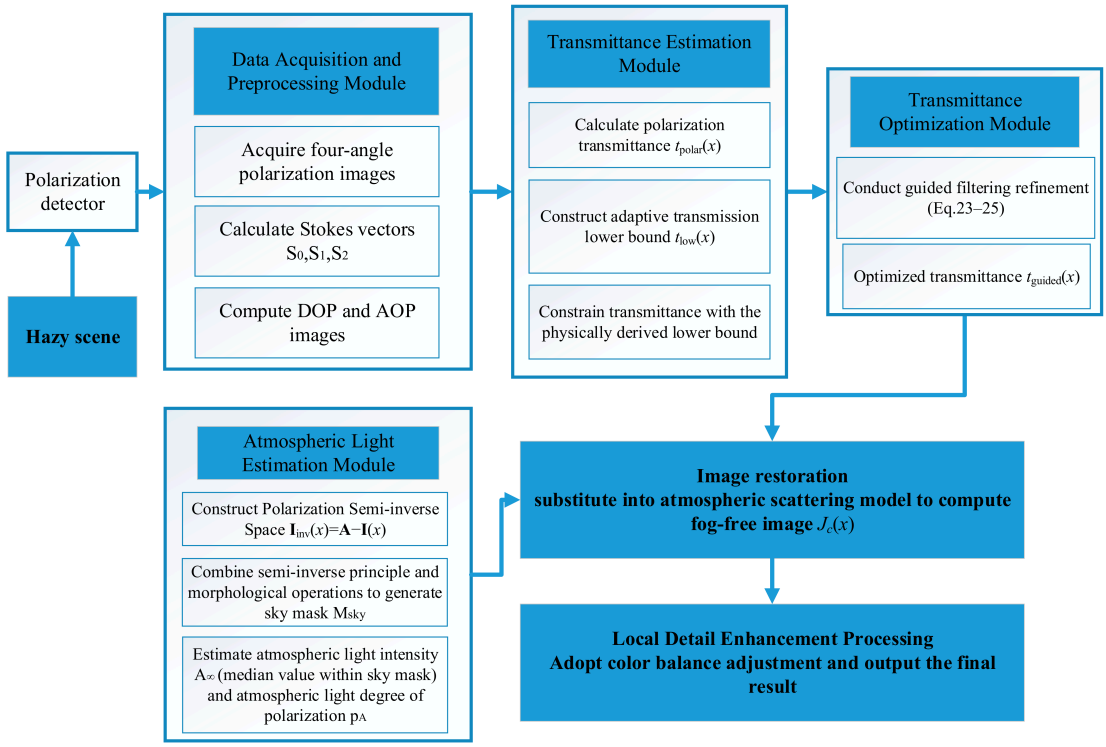



**Figure 1.** The proposed improved semi-inverse principle-based color polarization dehazing algorithm.

## 4. Experimental Design and Results Analysis

### *4.1. Experimental Data Acquisition and Parameter Settings*

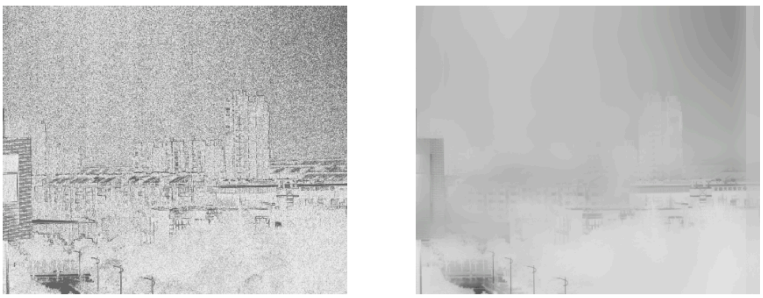
To verify the effectiveness of the proposed algorithm, an outdoor haze scene distant-target polarization imaging experimental platform was established [28]. The core imaging device employs a division-of-focal-plane color polarization camera (model TRI050S-QC, equipped with a Sony IMX250MZR sensor (Sony Corporation, Tokyo, Japan)). The camera has a resolution of 2448 × 2048 pixels and is capable of simultaneously capturing color images at four polarization angles (0°, 45°, 90°, and 135°). Its polarization measurement accuracy is ≤0.5°, which meets the requirements for distant-target polarization imaging. All experimental data were collected in real outdoor haze environments, covering conditions ranging from light to heavy haze, including urban scenes (buildings, roads, and distant targets), natural scenes (trees and distant mountain views), and water surface scenes (floating objects and shoreline distant targets). Multiple polarization image datasets were collected, each containing four images at different polarization angles, ensuring data diversity and representativeness. The experimental scenes are shown in Figure 2. In our experiments, the target distances are approximately 1.5–3.0 km. The visibility conditions correspond to dense haze, low-visibility conditions. Based on the target contrast and the degree to which distant objects are obscured, the visibility is estimated to be about 1.0–1.5 km, most likely around 1.2 km.

A comparison of the transmission map before and after guided filtering is shown in Figure 3 [19]. The original transmission map suffers from block artifacts and texture noise, resulting in blurred edges; after filtering, the map exhibits sharp and clear edges, with a naturally smooth transition in hazy regions. Noise interference is effectively suppressed while details at depth discontinuities are well preserved, thereby providing a high-precision transmission estimate for the subsequent image restoration.



(**a**) Distant hazy scene 1 (**b**) Distant hazy scene 2

**Figure 2.** Real captured scenes.



(**a**) Transmission map before filtering (**b**) Transmission map after filtering

**Figure 3.** Comparison of the transmission map before and after guided filtering.

Figure 4 visualizes the sky mask obtained directly from Equations (10)–(12). Panel (a) shows the input hazy image, panel (b) shows the semi-inverse feature map H(x), and panel (c) overlays the sky mask derived from Equations (10)–(12) on the input image, where the white region denotes the extracted sky area. As observed, the luminance-only coarse candidate mask from the semi-inverse transform tends to mistakenly select gray buildings, whereas the constraints defined in Equations (10)–(12) suppress such foreground interference, thereby retaining only sky regions while excluding buildings and roads.




(**i**) Real scene 1




(**ii**) Real scene 2

**Figure 4.** Visualization of sky mask generation pipeline. (**a**) Input hazy image; (**b**) semi-inverse feature map; (**c**) overlay of the final refined sky mask on the input image, where the white region represents the extracted sky area.

The core parameter settings of the proposed algorithm are as follows: the median of the total intensity in the sky region is taken as the atmospheric light intensity, with a lower

bound of 0.3; the degree of polarization of the atmospheric light is adjusted within the range [0.2, 0.95]; the lower and upper bounds of the transmission map are set to 0.35 and 0.95, respectively; the guided filtering radius is set to 50, with the regularization parameter $\varepsilon = 10^{-3}$; an enhancement factor of $\mu = 2.3$ is introduced into the restoration formula; the gamma correction coefficient is set to $\gamma = 0.7$; and CLAHE is adopted for local detail enhancement, with a clip limit of 0.015 and a tile size of $8 \times 8$. The purpose is to ensure that the parameter settings are scientifically sound and tailored to the requirements of the experimental scenes.

### *4.2. Experimental Results on Real-World Scenes*

To systematically verify the dehazing effectiveness and practical applicability of the proposed algorithm in real hazy environments, experiments on real-world scenes were conducted using the previously established experimental platform. Real images captured by the division-of-focal-plane color polarization camera were used as test samples, covering a variety of typical distant-target imaging scenarios. To ensure fairness and objectivity in the comparative experiments, the restored images of all algorithms under comparison, as well as those of the proposed algorithm, were post-processed using the same enhancement method with identical parameters, thereby eliminating the interference caused by differences in the enhancement steps, as shown in Figure 5. Since ground-truth haze-free reference images are unavailable for real outdoor hazy scenes, the experimental evaluation adopts both subjective visual assessment and non-reference objective quantitative metrics to compare the dehazing performance and target detail recovery capability of each algorithm.

Figure 5 presents the processing results of different algorithms on a real urban scene, with the original intensity image shown in Figure 5a. Seven representative mainstream dehazing algorithms are selected for comparison in the real-scene experiment, namely the dark channel prior method proposed by He et al. [12] (DCP, as shown in Figure 5b), the semi-inverse method proposed by Ancuti et al. [18] (Semi-Inverse, as shown in Figure 5c), the classical polarization-based dehazing method proposed by Schechner et al. [13] (Polar, as shown in Figure 5d), the polarization and dark channel fusion dehazing method proposed by Liang et al. [14] (P-DCP, as shown in Figure 5e), the atmospheric light estimation method using polarization degree gradient proposed by Zhao et al. [16] (PDG, as shown in Figure 5f), the sea fog image dehazing method based on pixel-level skylight polarization degree estimation proposed by Li et al. [17] (PSPD, as shown in Figure 5g), and the improved semi-inverse principle-based distant-target polarization dehazing algorithm proposed in this paper, as shown in Figure 5h. A multi-dimensional comparison of the processing results of these algorithms is conducted.

It can be observed that the DCP algorithm (Figure 5b) produces severe dark-edge artifacts and noticeable color noise in the sky region, with an overall bluish color cast. The Semi-Inverse algorithm (Figure 5c) suffers from large-area black block artifacts in the sky, resulting in a complete loss of distant scene information. The Polar algorithm (Figure 5d) leaves prominent color speckles in the sky region, and its performance heavily depends on the manual selection of the sky area. Liang's method (Figure 5e) improves the overall contrast but introduces severe chromatic noise (red and blue speckles) and unnatural color distortions. Zhao's method (Figure 5f) exhibits limited improvement in overall contrast, leaving the image relatively gray and the distant details blurred. The Li method (Figure 5g) tends to overexpose the sky region (resulting in a pure white sky), while the distant buildings are lost and the foreground colors become oversaturated, causing a harsh and unnatural transition between the sky and the ground objects. In contrast, the proposed method (Figure 5h) effectively suppresses the noise and artifacts in the sky region. It not only restores the contour details of distant buildings clearly but also preserves the natural

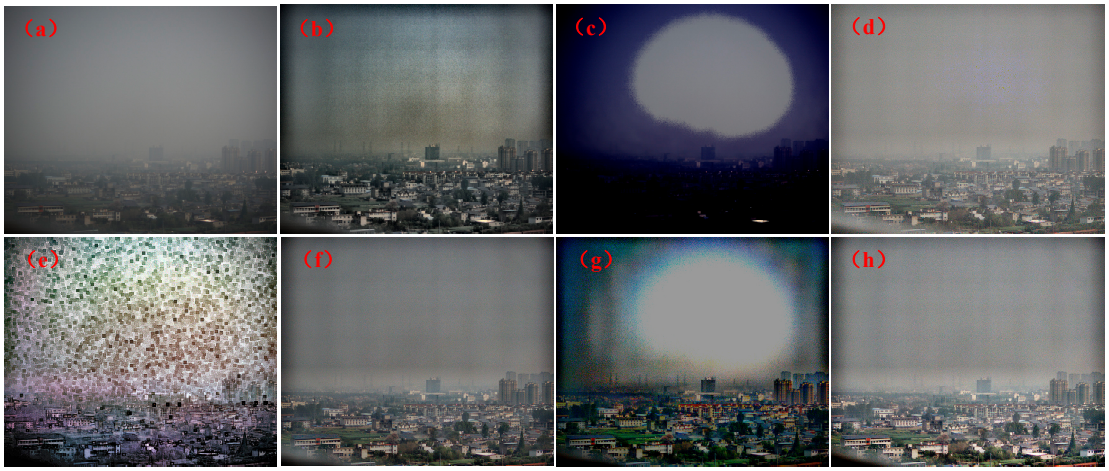
colors of the foreground vegetation, ensuring a smooth and visually pleasing transition in the sky region.




(**i**) Real scene 1




(**ii**) Real scene 2




(**iii**) Real scene 3

**Figure 5.** Processing results of three different real-world scenes: (**a**) original intensity image, (**b**) DCP [12], (**c**) Semi-Inverse [18], (**d**) Polar [13], (**e**) P-DCP [14], (**f**) PDG [16], (**g**) PSPD [17], (**h**) the proposed dehazing algorithm.

Table 1 summarizes the quantitative evaluation of real-scene images using six metrics: the local contrast enhancement metric (EME), Entropy, the Dehazed Image Quality

Index (DHQI), and the visible edges metric with its three sub-indicators—the rate of new visible edges (RNVE), the average gradient ratio (AGR), and the percentage of saturated pixels (PSP). Among these metrics, EME, Entropy, DHQI, RNVE, and AGR are positive indicators, for which larger values indicate better dehazing performance, whereas PSP is a negative indicator, for which a smaller value indicates less over-enhancement and clipping distortion. To quantitatively evaluate the performance of different dehazing algorithms, three representative real hazy scenes are selected, and the corresponding metric values of different methods are statistically analyzed.

**Table 1.** Quantitative comparison of different dehazing algorithms on real-world hazy scenes.

| Scene | Metrics | Raw | DCP | Semi-Inverse | Polar | Liang | Zhao | Li | Ours |
|---|---|---|---|---|---|---|---|---|---|
| Scene 1 | EME | 1.8783 | 8.1740 | 0.8529 | 9.1736 | 1.2989 | 10.396 | 10.3132 | 10.5206 |
| | Entropy | 7.5765 | 7.3086 | 5.7690 | 7.5388 | 7.5721 | 7.5097 | 4.0046 | 7.6087 |
| | DHQI | - | 0.2138 | 0.5041 | 0.0197 | 0.0092 | 0.0342 | 0.0297 | 0.3226 |
| | RNVE | - | 0.4804 | 0.3109 | 0.2333 | 0.2302 | 0.6401 | 0.4541 | 0.6649 |
| | AGR | - | 2.9164 | 1.5657 | 7.0261 | 12.5293 | 6.6479 | 6.8263 | 7.4730 |
| | PSP | - | 0.0152 | 0.3311 | 0.0041 | 0.0207 | 0.0034 | 0.5837 | 0.0029 |
| Scene 2 | EME | 2.4617 | 12.2867 | 0.1779 | 11.2534 | 2.0041 | 12.4166 | 9.0587 | 12.6613 |
| | Entropy | 7.2446 | 6.3531 | 3.3808 | 7.5941 | 7.2373 | 7.5263 | 5.2437 | 7.7305 |
| | DHQI | - | 0.4117 | 0.7180 | 0.0091 | 0.0082 | 0.0266 | 0.4797 | 0.0357 |
| | RNVE | - | 0.2956 | 0.6700 | 0.3438 | 0.3242 | 0.6992 | 0.2395 | 0.7090 |
| | AGR | - | 1.7249 | 1.2613 | 9.5187 | 13.0701 | 6.6979 | 2.0357 | 7.9983 |
| | PSP | - | 0.0244 | 0.6595 | 0.0127 | 0.0487 | 0.0007 | 0.3403 | 0.0006 |
| Scene 3 | EME | 1.0034 | 6.095 | 2.4645 | 4.8610 | 0.3874 | 6.3747 | 10.7430 | 8.1832 |
| | Entropy | 6.4994 | 7.8920 | 5.6511 | 6.6162 | 6.5580 | 6.6977 | 5.9679 | 7.0588 |
| | DHQI | - | 0.0807 | 0.2617 | 0.0244 | 0.0022 | 0.0161 | 0.0136 | 0.0270 |
| | RNVE | - | 1.8669 | 0.0319 | 0.5600 | 0.5639 | 2.1569 | 0.2757 | 2.1794 |
| | AGR | - | 4.2289 | 2.4675 | 5.7528 | 12.1654 | 7.1698 | 8.8712 | 10.3330 |
| | PSP | - | 0.0034 | 0.2110 | 0.1036 | 0.0490 | 0.0012 | 0.0019 | 0.0004 |

In Hazy Scene 1, the proposed method achieves the highest EME, representing a 2.01% increase compared to the next best method, Li. It also achieves the highest Entropy, a 0.43% increase over Raw, and the highest RNVE, a 3.87% increase over Zhao. It obtains the lowest PSP, a 14.71% decrease compared to Zhao. Its DHQI is higher than DCP by 50.89%, Polar by 1537.56%, Liang by 3406.52%, Zhao by 843.27%, and Li by 986.20%, though it is 36.00% lower than Semi-Inverse. Its AGR shows a 9.47% increase over Li and a 12.41% increase over Zhao, but is 40.35% lower than Liang. In Hazy Scene 2, the proposed method again obtains the highest EME, a 3.05% increase over DCP, the highest Entropy, a 1.80% increase over Polar, and the highest RNVE, a 1.40% increase over Zhao. It achieves the lowest PSP, a 14.29% decrease compared to Zhao. Its AGR is higher than most methods, showing a 19.41% increase over Zhao, but is 38.80% lower than Liang. However, its DHQI is lower than those of Semi-Inverse by 95.03%, Li by 92.56%, and DCP by 91.33%. It remains higher than Zhao by 34.21%, Polar by 292.31%, and Liang by 335.37%. In Hazy Scene 3, the proposed method achieves the highest RNVE, a 1.04% increase over Zhao, and the lowest PSP, a 66.67% decrease compared to Zhao. Its EME is higher than DCP by 34.25%, Semi-Inverse by 232.04%, Polar by 68.34%, Zhao by 28.37%, and Liang by 2012.34%, but lower than Li by 23.83%. Its Entropy is higher than Raw by 8.61%, Semi-Inverse by 24.91%, Polar by 6.69%, Liang by 7.64%, Zhao by 5.39%, and Li by 18.28%, but lower than DCP by 10.56%. Its AGR is higher than most methods, showing a 44.12% increase over Zhao, but is 15.06% lower than Liang. Its DHQI is higher than Li by 98.53% and Liang by 1127.27%, but lower than Semi-Inverse by 89.68% and DCP by 66.54%.

Overall, the proposed method consistently achieves the best EME, RNVE, and PSP values across all three scenes, and the best Entropy in Scenes 1 and 2. It also maintains competitive AGR and DHQI values. These results demonstrate that the proposed method effectively enhances local contrast, restores visible edges, and suppresses over-enhancement, while preserving information and overall quality in complex real-world hazy conditions.

Figure 6 presents a detailed comparison of distant scenes before and after dehazing. Before processing, distant targets are obscured by haze, with blurred edges and indistinguishable textures, resulting in low overall contrast. After processing with the proposed algorithm, the distant targets exhibit sharp edges and clearly discernible textures, with local details fully preserved. The algorithm effectively suppresses haze interference, significantly improving the detail visibility and contrast of distant targets.



(**a**) Original intensity image (**b**) Result of the proposed method

(**i**) Detail comparison of Scene 1



(**a**) Original intensity image (**b**) Result of the proposed method

(**ii**) Detail comparison of Scene 2



(**a**) Original intensity image (**b**) Result of the proposed method

(**iii**) Detail comparison of Scene 3

**Figure 6.** Detail comparison of distant scenes.

We evaluate the restoration performance within manually selected distant target ROIs using three metrics: target contrast, noise amplification, and edge fidelity. Target contrast is calculated as the standard deviation of pixel values inside the ROI, where higher values

indicate stronger target contrast. Noise amplification is defined as the ratio of the noise standard deviation of the dehazed image to that of the input hazy image within the ROI, and a smaller value means less noise amplification. Edge fidelity is computed as the Pearson correlation coefficient between the edge maps of the hazy input and the restored image in the ROI, and a value closer to 1 represents better preservation of real edges and fewer false edges.

Quantitative evaluations are performed within manually selected ROIs of distant targets across three real-world scenes, as listed in Table 2. In Scene 1, the target contrast rises from 0.1663 for the hazy input to 0.3715 for the restored image, representing a 123.4% improvement. In Scene 2, it increases from 0.3534 to 0.4152, a 17.5% improvement. In Scene 3, it rises from 0.0931 to 0.3616, a 288.4% improvement. These results verify that the proposed method substantially enhances the contrast of distant targets in all three scenes, especially in the low-contrast Scene 3. The noise amplification factors are 1.1735, 1.3406, and 2.4434 for Scenes 1, 2, and 3, respectively, indicating that noise in target regions is amplified during restoration, which is a well-known limitation of physics-driven dehazing approaches. The edge fidelity values are 0.3892, 0.5528, and 0.3646 for the three scenes, meaning that a considerable portion of target edges can be retained, albeit with slight edge distortion and minor artificial edges introduced during reconstruction. Overall, these results demonstrate that the proposed method effectively improves distant target contrast while maintaining reasonable edge preservation, though noise amplification remains an inherent challenge.

**Table 2.** Quantitative evaluation of restoration performance within manually selected distant target ROIs using target contrast, noise amplification, and edge fidelity.

| Scene | Image | Target Contrast | Noise Amplification | Edge Fidelity |
|---|---|---|---|---|
| Scene 1 | Original intensity image<br>proposed method | 0.1663<br>0.3715 | 1.1735 | 0.8892 |
| Scene 2 | Original intensity image<br>proposed method | 0.3534<br>0.4152 | 1.3406 | 0.7528 |
| Scene 3 | Original intensity image<br>proposed method | 0.0931<br>0.3616 | 2.4434 | 0.6646 |

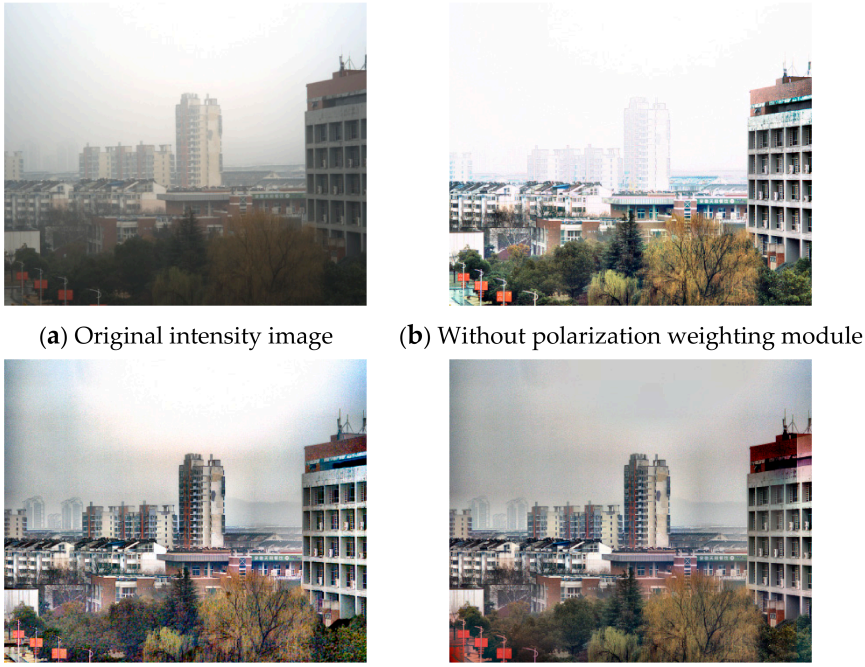
### *4.3. Ablation Study*

To verify the effectiveness of each module proposed in this paper, an ablation study is designed, as shown in Figure 7. On the real-world dataset, we tested three configurations separately: the one without the polarization weighting module, the one without the semi-inverse module, and the complete proposed algorithm, and compared their performance.

A combination of objective metrics and subjective evaluation is employed, with the statistical results presented in Table 3. The objective metrics include information entropy (Entropy), average gradient (AG), the measure of enhancement (EME), and the Dehazed Image Quality Index (DHQI).

The ablation study results demonstrate the individual and combined contributions of the polarization guidance and the semi-inverse modules. When the polarization guidance is removed (semi-inverse without polarization guidance), the algorithm relies solely on the semi-inverse principle. Although the AG and EME improve by approximately 415.9% and 347.2% compared with the original hazy image, the Entropy drops significantly by about 27.9%, indicating a severe loss of detailed information during restoration. When the semi-inverse module is removed (Polarization guidance without semi-inverse), the algorithm uses only polarization guidance. In this configuration, the Entropy remains nearly unchanged with a slight decrease of about 0.2%, while the AG and EME increase by approx-

imately 575.6% and 463.8%, respectively, showing that polarization guidance alone can effectively enhance contrast and gradient information. However, its DHQI is about 11.0% lower than that of the semi-inverse-only configuration. In contrast, the proposed complete algorithm achieves the best performance in three of the four metrics. It attains the highest Entropy (an increase of about 1.2% over the original), the highest AG (an increase of about 598.8%), and the highest EME (an increase of about 469.4%), demonstrating superior detail preservation, gradient enhancement, and local contrast improvement. Its DHQI is about 4.6% lower than that of the semi-inverse-only configuration, but about 7.3% higher than that of the polarization-only configuration. This suggests that while the complete algorithm significantly strengthens detail recovery and contrast, the DHQI metric may reflect a trade-off related to perceptual quality or minor over-enhancement, yet it still outperforms the polarization-only configuration in overall quality. Overall, these experimental results verify that polarization guidance and the semi-inverse principle complement each other and are both indispensable for ensuring the clarity, contrast, and information integrity of distant-target dehazing.



(**a**) Original intensity image (**b**) Without polarization weighting module

(**c**) Without semi-inverse module (**d**) Complete algorithm module

**Figure 7.** Ablation verification experiment of the proposed method.

**Table 3.** Comparison results of the ablation study.

| Configuration | Entropy | AG | EME | DHQI |
|---|---|---|---|---|
| Original hazy image | 7.2664 | 0.0082 | 1.8869 | - |
| Semi-inverse without polarization guidance | 5.2426 | 0.0423 | 8.4397 | 0.0263 |
| Polarization guidance without semi-inverse | 7.2551 | 0.0554 | 10.6384 | 0.0234 |
| Complete algorithm | 7.3565 | 0.0573 | 10.7427 | 0.0251 |

### *4.4. Comparison Under Different Hazy Conditions*

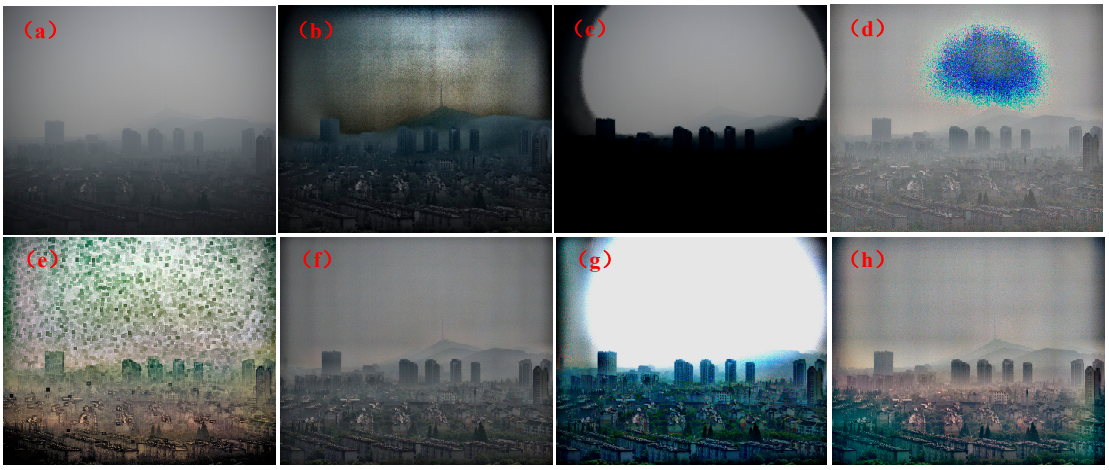
To verify the effectiveness and robustness of the proposed method, comparative experiments are conducted under thin, medium, and heavy haze conditions, as shown in Figure 8.




(**i**) Real scene 1—thin haze conditions




(**ii**) Real scene 2—medium haze conditions




(**iii**) Real scene 3—heavy haze conditions

**Figure 8.** Processing results under low, moderate and heavy haze conditions: (**a**) is the original intensity image, (**b**) DCP [12], (**c**) Semi-Inverse [18], (**d**) Polar [13], (**e**) P-DCP [14], (**f**) PDG [16], (**g**) PSPD [17], (**h**) the proposed dehazing algorithm.

Visual comparison in Figure 8 further confirms these quantitative findings. The proposed method effectively restores distant building contours, preserves natural colors, and suppresses the severe artifacts, color casts, and noise amplification observed in DCP, Semi-Inverse, Polar, Liang, and Zhao. Compared with Li's method, which achieves high EME in some scenes, the proposed method provides more consistent detail preservation and edge

recovery. These results demonstrate that the proposed method is both effective and robust for sea fog image dehazing under thin, medium, and heavy haze conditions.

As shown in Table 4, in the thin haze scene, compared with the raw hazy image, the proposed method improves EME and Entropy by 481.2% and 1.8%, respectively. It also achieves the highest RNVE and AGR, with improvements of 2.0% and 21.1% over the second-best method, while maintaining a low PSP. In the medium haze scene, EME and Entropy are improved by 673.3% and 1.7% over the raw image, and the highest RNVE is 1.3% higher than the second-best method, with AGR and PSP remaining competitive. In the heavy haze scene, EME and Entropy increase by 984.6% and 3.9% over the raw image, and the highest RNVE and AGR are 2.3% and 15.7% higher than the second-best method, with PSP kept at a low level. Although DHQI is not always the highest, the overall performance is balanced and superior across varying haze densities.

**Table 4.** Statistics of six quantitative metrics for real-world scenes with different dehazing algorithms.

| Scene | Metrics | Raw | DCP | Semi-Inverse | Polar | Liang | Zhao | Li | Ours |
|---|---|---|---|---|---|---|---|---|---|
| Scene 1-thin haze conditions (薄雾) | EME | 1.4540 | 6.9810 | 1.0734 | 7.5925 | 0.8590 | 7.7178 | 9.4728 | 8.4502 |
| | Entropy | 7.4386 | 7.2895 | 5.6125 | 7.4112 | 7.4604 | 7.3232 | 4.3085 | 7.5722 |
| | DHQI | - | 0.1000 | 0.0304 | 0.0093 | 0.0045 | 0.0236 | 0.0303 | 0.0325 |
| | RNVE | - | 0.6547 | 0.3134 | 0.2994 | 0.2985 | 0.8855 | 0.4185 | 0.9036 |
| | AGR | - | 3.4842 | 1.6203 | 7.8809 | 12.2732 | 6.1301 | 8.2549 | 14.8605 |
| | PSP | - | 0.0127 | 0.3281 | 0.0039 | 0.0333 | 0.0002 | 0.0005 | 0.0007 |
| Scene 2-medium haze conditions (中雾) | EME | 1.0084 | 5.8976 | 1.9074 | 5.9049 | 0.4554 | 6.0695 | 8.0296 | 7.7988 |
| | Entropy | 7.1351 | 7.0036 | 6.1547 | 7.1180 | 7.1776 | 7.0324 | 3.6097 | 7.2554 |
| | DHQI | - | 0.0786 | 0.4785 | 0.0093 | 0.0038 | 0.0221 | 0.0262 | 0.0303 |
| | RNVE | - | 1.0048 | 0.1366 | 0.3696 | 0.3658 | 1.2733 | 0.4709 | 1.2904 |
| | AGR | - | 4.1705 | 1.8012 | 8.0140 | 10.5464 | 6.7418 | 9.6435 | 9.3908 |
| | PSP | - | 0.0066 | 0.2028 | 0.0052 | 0.0366 | 0.0004 | 0.0004 | 0.004 |
| Scene 3-heavy haze conditions (浓雾) | EME | 0.8921 | 4.6824 | 1.5918 | 5.9353 | 0.2778 | 5.4632 | 12.0061 | 9.6758 |
| | Entropy | 7.0562 | 7.2465 | 4.8953 | 6.9932 | 7.0999 | 6.8904 | 5.0602 | 7.3307 |
| | DHQI | - | 0.0319 | 0.3345 | 0.0027 | 0.0023 | 0.0143 | 0.0144 | 0.0145 |
| | RNVE | - | 1.5310 | 0.2343 | 0.5732 | 0.5683 | 2.0973 | 0.0979 | 2.1451 |
| | AGR | - | 4.6910 | 2.0639 | 11.9549 | 19.3601 | 6.7807 | 10.3056 | 22.3905 |
| | PSP | - | 0.0113 | 0.3871 | 0.0050 | 0.0307 | 0.0003 | 0.0002 | 0.0008 |

### *4.5. Discussion*

To quantitatively evaluate the reliability of the proposed sky mask extraction, we define the foreground contamination ratio as the percentage of non-sky foreground pixels remaining in the final refined sky mask and test two categories of hazy scenes. The average foreground contamination ratios are 4.2% for bright-sky scenes (15 images) and 7.1% for sky-free scenes (12 images). The mean relative errors between the estimated and manually annotated atmospheric light are 3.8% and 6.7%, respectively. These low values demonstrate that the two-stage screening strategy effectively suppresses foreground interference and ensures robust atmospheric-light estimation, as the polarization prior helps reject gray foreground objects whose polarization difference is much smaller than that of hazy sky.

The study finds that as $t_{\min}$ increases from 0.1 to 0.4, the brightness of distant scenes gradually improves; however, when it exceeds 0.4, the overall image becomes overly bright and the haze appearance intensifies, making 0.35 the optimal value. The enhancement factor of $\mu$ produces good results in the range of 1.8 to 2.8, with 2.3 as the best balance point. A guided filtering radius smaller than 20 cannot effectively smooth texture noise, while a value larger than 100 leads to over-smoothing and edge blurring; a radius of 50 is suitable for most scenes. A CLAHE clip limit of 0.015 can suppress noise, whereas increasing it to

0.03 leads to a noticeable increase in noise. The transmission floor precedes fusion, gamma correction and CLAHE are adaptively controlled by estimated fog density and polarization confidence and embedded in fusion, not sequential post-processing.

The core contribution of this work lies in the first deep integration of the improved semi-inverse principle with color polarization imaging, achieving systematic improvements in three key aspects: adaptive atmospheric light estimation, transmission fusion optimization, and physics-based color constraints. The algorithm not only maintains the rigor of the physical model but also overcomes the shortcomings of traditional methods in terms of automation, noise suppression, and color fidelity, providing a new solution with both theoretical depth and practical value for high-quality imaging in complex environments. Compared with current mainstream methods, the distinctive positioning of this research is clear. Compared with the methods of He and Ancuti, this work introduces polarization information into the semi-inverse framework for the first time, overcoming the limitations of single-image statistical priors under complex illumination conditions. Compared with Schechner's method and its variants, the improved semi-inverse principle replaces the manual selection of the sky region, and for the first time systematically addresses the issue of color fidelity in polarization-based dehazing. Compared with deep learning-based dehazing methods, this work does not rely on large-scale training data, possesses stronger physical interpretability and scene generalization capability, and is more advantageous in real-world application scenarios where paired data are unavailable. Real-world experiments on hazy scenes have been conducted, verifying the effectiveness and superiority of the proposed algorithm.

Although the proposed algorithm has achieved good results, it still has the following limitations: (1) The computational complexity is relatively high; operations such as clustering analysis and guided filtering make it difficult to meet real-time processing requirements on embedded platforms. Future work may consider algorithm lightweighting or hardware acceleration. (2) Under extremely dense fog conditions with visibility below 50 m, the accuracy of atmospheric light estimation decreases, limiting the dehazing performance. (3) The images used in this study were acquired during daytime under fog conditions. It should be noted that the solar position can influence the skylight polarization pattern and may therefore affect the imaging results. In our experiments, the acquisition time was kept relatively stable, and the variation in solar position was limited, which helps maintain consistency in the polarization observations. Nevertheless, this factor may still introduce a certain influence on the dehazing performance, and the current results should be interpreted with this condition in mind. Future work will consider more diverse acquisition times and solar positions to further validate the generality and robustness of the proposed algorithm. This limitation and the corresponding future direction are also discussed as part of the scope of this study.

## 5. Conclusions

This paper proposes a color polarization dehazing algorithm based on an improved semi-inverse principle. By deeply integrating the semi-inverse principle with the physical properties of polarization imaging, the algorithm achieves pixel-wise adaptive estimation of atmospheric light parameters and refined optimization of the transmission map. The main contributions include: constructing a semi-inverse transformation model in the polarization space, enabling adaptive estimation of the polarization characteristics of atmospheric light using Stokes parameters; designing a guided-filtering-based refined transmission estimation method that effectively suppresses noise amplification in low-polarization regions; and the transmittance is estimated by exploiting the relationship between the polarization difference within the sky mask and the degree of polarization of atmospheric

light. Experimental results demonstrate that the proposed algorithm outperforms existing mainstream algorithms in both objective metrics and subjective visual quality, providing an effective solution for high-quality imaging in complex environments. Future research will focus on improving the computational efficiency of the algorithm and enhancing its adaptability to dynamic scenes, so as to further elevate the dehazing performance.

**Author Contributions:** Conceptualization, Q.S. and T.Y.; methodology, M.Z.; software, Q.S.; validation, Q.S. and M.Z.; formal analysis, M.Z.; investigation, Q.S., D.M. and T.Y.; resources, Q.S.; data curation, Q.S. and M.Z.; writing—original draft preparation, Q.S.; writing—review and editing, Q.S.; visualization, Q.S.; supervision, M.Z., D.M., T.Y. and Y.S.; project administration, Q.S.; funding acquisition, Q.S., D.M. and T.Y. All authors have read and agreed to the published version of the manuscript.

**Funding:** This work was supported by the National Natural Science Foundation of China (Grant No. 42305140); Anhui Provincial Key Research and Development Program (Grant No. 2022a05020010); Key Project for Scientific Research of Anhui Provincial Universities (Grant No. 2024AH051728); Enterprise-entrusted Horizontal R&D Projects (Grant Nos. 2023HX271, 2025HX570).

**Data Availability Statement:** The data presented in this study are available on request from the first author.

**Conflicts of Interest:** The authors declare no conflicts of interest.

## References

1. Ju, M.Y.; Ding, C.; Ren, W.Q.; Yang, Y.; Zhang, D.Y.; Guo, Y.J. IDE: Image Dehazing and Exposure Using an Enhanced Atmospheric Scattering Model. *IEEE Trans. Image Process.* **2021**, *30*, 2180–2192. [CrossRef] [PubMed]
2. Fattal, R. Dehazing using color-lines. *ACM Trans. Graph.* **2014**, *34*, 1–14. [CrossRef]
3. Liu, Y.; Chen, X.; Wang, Z.; Liu, F. Multi-scale polarization dehazing network based on physical prior. *Opt. Express* **2021**, *29*, 14827–14846.
4. Wang, W.; Yuan, X.; Wu, X.; Liu, Y. Fast Image Dehazing Method Based Linear Transformation. *IEEE Trans. Multimed.* **2017**, *19*, 1142–1155. [CrossRef]
5. Jiang, S.; Mei, Y.; Wang, P.; Liu, Q. Exposure difference network for low-light image enhancement. *Pattern Recognit.* **2024**, *156*, 10. [CrossRef]
6. Yang, K.; Liu, F.; Liang, S.; Xiang, M.; Han, P.; Liu, J.; Dong, X.; Wei, Y.; Wang, B.; Shimizu, K.; et al. Data-driven polarimetric imaging: A review. *Opto-Electron. Sci.* **2024**, *3*, 230042. [CrossRef]
7. Wang, X.; Han, P.; Luo, X.; Liu, Q.; Zhang, T.; Dong, X.; Xiang, M.; Liu, J.; Liu, Y.; Liu, F. Scene-level passive polarization 3D imaging. *Opto-Electron. Adv.* **2026**, *9*, 5–11. [CrossRef]
8. Shen, L.; Zhang, L.; Qi, P.; Zhang, X.; Li, X.; Huang, Y.; Zhao, Y.; Hu, H. Polarimetric binocular three-dimensional imaging in turbid water with multi-feature self-supervised learning. *PhotoniX* **2025**, *6*, 24. [CrossRef]
9. Luo, X.; Wang, X.; Han, P.; Liu, J.; Liu, Y.; Zhang, T.; Liu, F. Polarization-guided three-dimensional recovery through scattering media. *Opt. Lett.* **2026**, *51*, 1235–1238. [CrossRef] [PubMed]
10. Liu, Q.; Park, J.; Han, P.; Ji, X.; Guan, R.; Xin, R.; Han, T.; Dong, X.; Zhang, T.; Xiang, M.; et al. Polarization 3D imaging: Principles, applications, and challenges. *Adv. Imaging* **2026**, *3*, 032003. [CrossRef]
11. Luo, X.; Wang, S.; Liu, J.; Dong, X.; He, P.; Yang, Q.; Chen, X.; Zhou, F.; Zhang, T.; Feng, S.; et al. Revolutionizing optical imaging: Computational imaging via deep learning. *Photonics Insights* **2025**, *4*, R03. [CrossRef]
12. He, K.; Sun, J.; Tang, X. Single image haze removal using dark channel prior. *IEEE Trans. Pattern Anal. Mach. Intell.* **2011**, *33*, 2341–2353. [CrossRef] [PubMed]
13. Schechner, Y.Y.; Narasimhan, S.G.; Nayar, S.K. Polarization-based vision through haze. *Appl. Opt.* **2003**, *42*, 511–525. [CrossRef] [PubMed]
14. Liang, J.; Ren, L.; Ju, H.; Zhang, W.; Qu, E. Polarimetric dehazing method for dense haze removal based on distribution analysis of angle of polarization. *Opt. Express* **2017**, *25*, 26146–26159.
15. Feng, S.; Chen, Q.; Gu, G.; Sui, X.; Gao, H. Polarization-based haze removal using self-adaptive guided filter. *Appl. Opt.* **2019**, *58*, 1753–1763.
16. Zhao, J.; Zhang, Z.; Zhu, Y.; Zhang, Z. Atmospheric Light Estimation Using Polarization Degree Gradient for Image Dehazing. *Sensors* **2024**, *24*, 3137. [CrossRef] [PubMed]

17. Li, L.; Geng, L.; He, Z.; Liu, D.; Jin, J.; Dai, Y.; Xu, H.; Li, K. A dehazing method for sea fog images based on pixel-level skylight polarization degree estimation. *J. Mod. Opt.* **2024**, *71*, 157–171. [CrossRef]
18. Ancuti, C.O.; Ancuti, C.; Hermans, C.; Bekaert, P. A Fast Semi-inverse Approach to Detect and Remove the Haze from a Single Image. In *Asian Conference on Computer Vision*; Springer: Berlin/Heidelberg, Germany, 2011.
19. Parnet, F.; Fade, J.; Ortega, Q.N.; Loas, H.; Frein, L.; Alouini, M. Freespace active polarimetric imager operating at 1.55 μm by orthogonality breaking sensing. *Opt. Lett.* **2017**, *42*, 723–726. [CrossRef] [PubMed]
20. Shen, L.; Zhao, Y.; Peng, Q.; Chan, J.C.-W.; Kong, S.G. An iterative image dehazing method with polarization. *IEEE Trans. Multimed.* **2019**, *21*, 1093–1107. [CrossRef]
21. Liang, J.; Ju, H.; Ren, L.; Yang, L.; Liang, R. Generalized polarimetric dehazing method based on low-pass filtering in frequency domain. *Sensors* **2020**, *20*, 1729. [CrossRef] [PubMed]
22. Wang, C.; Zhao, K. Polarization image defogging based on dark channel prior principle. *Opt. Precis. Eng.* **2023**, *31*, 3474–3481. [CrossRef]
23. Sun, R.; Liao, T.; Fan, Z.; Zhang, X.; Wang, C. Polarization dehazing method based on separating and iterative optimizing airlight from the frequency domain for different concentrations of haze. *Appl. Opt.* **2022**, *61*, 10362–10373. [CrossRef] [PubMed]
24. Zhu, Q.; Mai, J.; Shao, L. A fast single image haze removal algorithm using color attenuation prior. *IEEE Trans. Image Process.* **2015**, *24*, 3522–3533. [CrossRef] [PubMed]
25. He, K.; Sun, J.; Tang, X. Guided image filtering. *IEEE Trans. Pattern Anal. Mach. Intell.* **2012**, *35*, 1397–1409. [CrossRef] [PubMed]
26. Zhang, X.; Song, M.; Fan, Z.; Jin, H. Reconstruction algorithm of haze image based on blind separation model of polarized orthogonal airlight. *Opt. Express* **2022**, *30*, 42097–42113. [CrossRef] [PubMed]
27. Choi, L.K.; You, J.; Bovik, A.C. Referenceless prediction of perceptual fog density and perceptual image defogging. *IEEE Trans. Image Process.* **2015**, *24*, 3888–3901. [CrossRef] [PubMed]
28. Sun, R.; Chen, L.; Liao, T.; Fan, Z. Self-supervised polarization image dehazing method via frequency domain generative adversarial networks. *Pattern Recognit.* **2025**, *165*, 111615. [CrossRef]


**Disclaimer/Publisher's Note:** The statements, opinions and data contained in all publications are solely those of the individual author(s) and contributor(s) and not of MDPI and/or the editor(s). MDPI and/or the editor(s) disclaim responsibility for any injury to people or property resulting from any ideas, methods, instructions or products referred to in the content.